Results in Physics 8 (2018) 128–139

Contents lists available at ScienceDirect

Results in Physics

journal homepage: www.journals.elsevier.com/results-in-physics

Synthesis, structural and electrical studies of $Ba_{1-x}Sr_xCe_{0.65}Zr_{0.25}Pr_{0.1}O_{3-\delta}$ electrolyte materials for solid oxide fuel cells

J. Madhuri Sailaja [a], N. Murali [a,b,*], S.J. Margarette [a], Tulu Wegayehu Mammo [a], V. Veeraiah [b]

[a] Department of Physics, Andhra University, Visakhapatnam, Andhra Pradesh, India
[b] Advanced Analytical Laboratory, DST-PURSE Programme, Andhra University, India

ARTICLE INFO

Article history:
Received 26 October 2017
Received in revised form 25 November 2017
Accepted 25 November 2017
Available online 2 December 2017

Keywords:
Solid oxide fuel cell
Proton conducting electrolyte
Chemical stability
Sol–gel synthesis
$BaCeO_3$

ABSTRACT

This paper is discussed Sr doping effect on the microstructure, chemical stability and conductivity of $Ba_{1-x}Sr_xCe_{0.65}Zr_{0.25}Pr_{0.1}O_{3-\delta}$ ($0 \le x \le 0.2$) electrolyte prepared by sol–gel method. The lattice constants and unit cell volumes are found to decrease as Sr atomic percentage increased in accordance with the Vegard law, confirming the formation of solid solution with orthorhombic structure. Among them all the synthesized samples are showed a conductivity with different atmosphere values at 500 °C. $Ba_{0.92}Sr_{0.08}Ce_{0.65}Zr_{0.25}Pr_{0.1}O_{3-\delta}$ recorded highest conductivity with a value of 3.3×10^{-6} S/cm (dry air) & 3.41×10^{-6} S/cm (wet air with 3% relative humidity) at 500 °C due to its smaller lattice volume, larger grain size and lower activation energy that led to excessive increase in conductivity. All pellets exhibited good chemical stability when exposed to air and H_2O atmospheres. This study elucidates that the composition will be a promising electrolyte material for use as SOFC at intermediate temperatures if Sr doping is limited to small amounts.

Introduction

$BaCeO_3$ based ceramic materials are one of the protons conducting perovskite oxides to show relatively high electrical conductivity when compared to other perovskite zirconates [1–6]. These oxides are mostly used as the electrolytes in fuel cells, hydrogen pumps and gas sensors [7–12]. At operating temperatures, the electrolyte should satisfy the condition of material having dense structure in order to avoid the mixing between the gases coming from both anode and cathode. Many efforts are focussed to obtain dense samples at lower temperatures either by doping Zr, Y, Yb, Gd or by adding non refractory oxides like ZnO. The electrical transport properties are strongly influenced by size and conductivity of the grains. Thus the microstructure is the key to improve the condition through the bulk and the grain boundary.

In contrast to $BaCeO_3$, $BaZrO_3$ is stable under CO_2 and under humid reductive conditions. Partial substitution of Ce^{4+} with Zr^{4+} provided a partly substituted $Ba(CeZr)O_3$ with better stability but on the other hand conductivities achieved are not still sufficient for commercial applications where power densities over 0.1 W/cm^2 are required [13–15]. Among them the available materials, Praseodymium is a soft, malleable, silvery and ductile material in the lanthanide group and valued for its magnetic, chemical and optical properties like more rare earth elements. It readily forms trivalent Pr (III) ions and more resistant to corrosion in air than europium (Eu), lanthanum (La), cerium (Ce) or neodymium (Nd) with oxidation states +2, +3 and +4. Pr and Ce ions have very similar crystal structure, chemical properties and consequently are compatible in the perovskite crystal structure. Pr readily forms materials containing more than one oxidation state, or so more than cerium, zirconium surpasses the ability for electrochemical activity through transitions between oxidation states of adjacent Pr centers within the lattice. It has been recently shown that perovskite materials doped with praseodymium manifests relatively high conductivity at low and intermediate temperatures. In particular $BaPr_{(1-g)}Gd_gO_3$ exhibits conductivity ranging from 5×10^{-3} S/cm at 200 °C to 0.5 S/cm at 700 °C that depicted higher values than the benchmark barium cerates [16–22].

The electrical conductivity of $BaCe_{0.8}Pr_{0.2}O_{3-\delta}$ was found to be 3.07×10^{-4} S/cm at 600 °C with a sintering temperature of 1350 °C/12 h [23]. A recent study indicated that introduction of Pr as a dopant in BZY did not reduce its electrical performance. Fabbri et al., developed $BaZr_{0.7}Pr_{0.1}Y_{0.2}O_{3-\delta}$ nano structured powders by a combustion method which dramatically improved the sinterability of BZY material with a conductivity of order of 10^{-2} S/cm [24].

Thermodynamically $SrCeO_3$ is more stable than $BaCeO_3$ and very few research papers dealt with $BaSrCeZrO_3$ structures. Thus the present work is aimed to study the effect of strontium by

* Corresponding author at: Advanced Analytical Laboratory, DST-PURSE Programme, Andhra University, India.
E-mail address: murali.nandigam1@gmail.com (N. Murali).

https://doi.org/10.1016/j.rinp.2017.11.032
2211-3797/

partially replacing Ba in the A sites along with co-doping strategy of Pr in B sites of barium cerate- zirconates and examine the chemical stability and conductivity.

Experimental

Powder preparation

The citrate-EDTA complexing sol–gel process is employed for preparing $BaCe_{0.9}Pr_{0.1}O_{3-\delta}$ (BCP), $BaCe_{0.65}Zr_{0.25}Pr_{0.1}O_{3-\delta}$ (BCZP) and $Ba_{1-x}Sr_xCe_{0.65}Zr_{0.25}Pr_{0.1}O_3$ (BSCZP-1 to BSCZP-4) x = 0.04, 0.08, 0.16, 0.2) oxides. The starting materials were commercial $Ba(NO_3)_2$, $ZrO(NO_3)_2{\cdot}2H_2O$, $Ce(NO_3)_3{\cdot}6H_2O$ (High Media, 99.5%), Sr $(NO_3)_2$, $Pr(NO_3)_3{\cdot}6H_2O$ (Sigma Aldrich). Both citric acid and EDTA perform the operation of chelating agents to the precursor solution. The ratio of molar solutions of EDTA: citric acid: total metal cations content is set at 1:2:1. The pH value of the solution is adjusted to be ~6 by addition of small amounts of NH_4OH. The mixed solutions were heated to 100 °C under continuous stirring over night to remove excess water and promote polymerisation. During continuous heating, the solution becomes more viscous with a change of colour from colourless to dark brown gel form. On further heated to a temperature of 250 °C/24 h in an oven to evaporate residual water and organics, these gels get converted into black powders. The synthesized powders are now calcined at 1100 °C (12 h) with a heating rate of 5 °C/min. All the samples are coloured in yellow colour which is marked in contrast to the Pr doped materials of chocolate in colour. To obtain dense samples, the resulted fine calcined powders were uniaxially pressed into cylindrical pellets at 5 ton pressure and then sintered (at 1300 °C for 5 h at a heating rate of 5 °C min^{-1}) in air atmosphere. While sintering small amount of powder is sprinkled on the platinum foil to avoid material evaporation in the process.

Characterization

Thermogravimetric analysis (TGA) is carried out to the dried powder (T = 250 °C) by a TA instrument model SDT Q600. The phase identification of the sintered oxides is analysed with a powder diffractometer (PANalytical X-pert Pro) with Ni filtered Cu-Kα radiation and the diffraction angle from 10° to 90° with an interval of 0.01°/min. Morphologies of the sintered pellets are examined using Scanning Electron Microscope (JEOL model JSM-6610 LV) in combination with an Energy Dispersion Spectrometer (EDS) to estimate the percentage of elements present in the samples. A FTIR spectrometer (SHIMADZU IR Prestige-21, Singapore) is employed to record the Fourier transform infrared (FTIR) spectra of calcined and sintered BCP, BCZP and $Ba_{1-x}Sr_x$ $Ce_{0.65}Zr_{0.25}Pr_{0.1}O_{3-\delta}$ powder in the range of 4000–400 cm^{-1} to predict the complex, carbonates and oxides formation. The theoretical density of the powders is calculated with the obtained XRD. Fourier transforms Raman spectroscopy is employed to study the vibrational modes of the samples in the range 0–1200 cm^{-1}. LCR measurements from room temperature to 500 °C (in dry air and wet air with 3% relative humidity) are performed with (Wayneker P65000 model and Solatron 1260) in the frequency range from 20 to 1 MHz. Silver paste is painted on both sides of the pellet and heated in a furnace at 375 °C for half an hour prior to Impedance measurements.

Results and discussion

Thermo gravimetry/differential thermal analysis (TG-DTA)

To evaluate the reaction during the formation of the perovskite phase structure, simultaneous TG-DTA curves of the samples are conducted from room temperature to 1200 °C. Thermal studies reveal that there are three major steps in the decomposition process. They are (1) loss of moisture (b) decomposition of nitrates to corresponding oxides (c) solid state diffusion reaction leading to the formation of perovskite.

Three regions are reflected in TG-DTA of the powder as shown in Fig. 1(a)–(f). The gradual weight loss up to 100 °C with corresponding endothermic peaks are due to absorption of water molecules that arises due to storage of preheated sample in the ambient atmosphere. The further weight loss accompanied by two exothermal peaks in DTA reveals that the decomposition of gel takes place in two steps. The weight loss from 100 to 500 °C accompanied with small exothermic peak near 300–550 °C which may be due to thermal decomposition of the citrate complex, burning of citrate chains and metal nitrates. The weak endothermic peak near 800 °C can be ascribed to a polymorphic phase transformation from orthorhombic to hexagonal in $BaCeO_3$. The weight loss from 500 to 1000 °C and the exothermic peaks near 900 °C is due to co-oxidation [25]. A very small weight loss is observed above 1050 °C which is due to thermal decomposition of barium carbonate, with the release of CO_2 for all the samples and formation of perovskite phase [26–28]. This is consistent with the XRD results that $Ba_{1-x}Sr_xCe_{0.65}Zr_{0.25}Pr_{0.1}O_{3-\delta}$ phase only forms upon calcining at 1100 °C and above. There is no noticeable weight change when the temperature is higher than 1100 °C, indicating that complete decomposition of $BaCO_3$ and formation of $BaSr_xCe_{0.65}Zr_{0.25}Pr_{0.1}O_{3-\delta}$ compound. A small amount of weight gain is observed above 1100 °C for samples which may be due to the formation of $BaCO_3$ or $SrCeO_3$ like second phase or due to buoyancy effect owing to the decreasing density of the purge gas (Ar) with temperature. Individual decomposition of the compound with respect to heat treatment is illustrated below in Table 1.

Deanello et al. [29] studied the effect of pH on CeO_2 precipitation for the $Sr_{0.85}Ce_{0.15}FeO_{3-x}$ perovskite system processed by solution combustion synthesis with citric acid and showed that segregation of CeO_2 is substantially reduced with increasing pH. The phase formation in sol gel method may be attributed to the chelating strength of citric acid towards metal ions at different pH conditions. Acids generally dissociated and liberate protons, where ligands can form metal complexes citric acid is a polyprotic acid (H_3A) which has three dissociation constants namely Pk_{a1} (3.10), Pk_{a2} (4.77) and pk_{a3} (6.4) liberating three protons [29,30] as shown in equations below.

$$\text{At}pK_{a1} \qquad H_3A \rightarrow H^+ + H_2A^- \tag{1}$$

$$\text{At}pK_{a2} \qquad H_2A^- \rightarrow H^+ + HA^{2-} \tag{2}$$

$$\text{At } pK_{a3} \qquad HA^{2-} \rightarrow H^+ + A^{3-} \tag{3}$$

A low pH level (1), the precursor solution is not sufficient to dissociate citric acid and hence the tendency to form metal complexes is lower. On increasing the pH further to 6, liberates the PK_{a2} (4.77) and PK_{a3} (6.4) protons respectively and this further enhances the concentration of metal complex in the solution which favours the formation of the desired phase. Moreover, NH_4OH which is added for controlling pH of the precursor solution, separates to from bonds with nitrate ions and results in the formation of NH_4NO_3 [31]. This compound acts as an additional oxidizer which can further improve the efficiency of combustion reaction.

XRD analysis

The formation of multi component perovskite oxide involves the rearrangement of oxygen ions and cations during the process of synthesis. As solid state reaction requires high calcination tem-

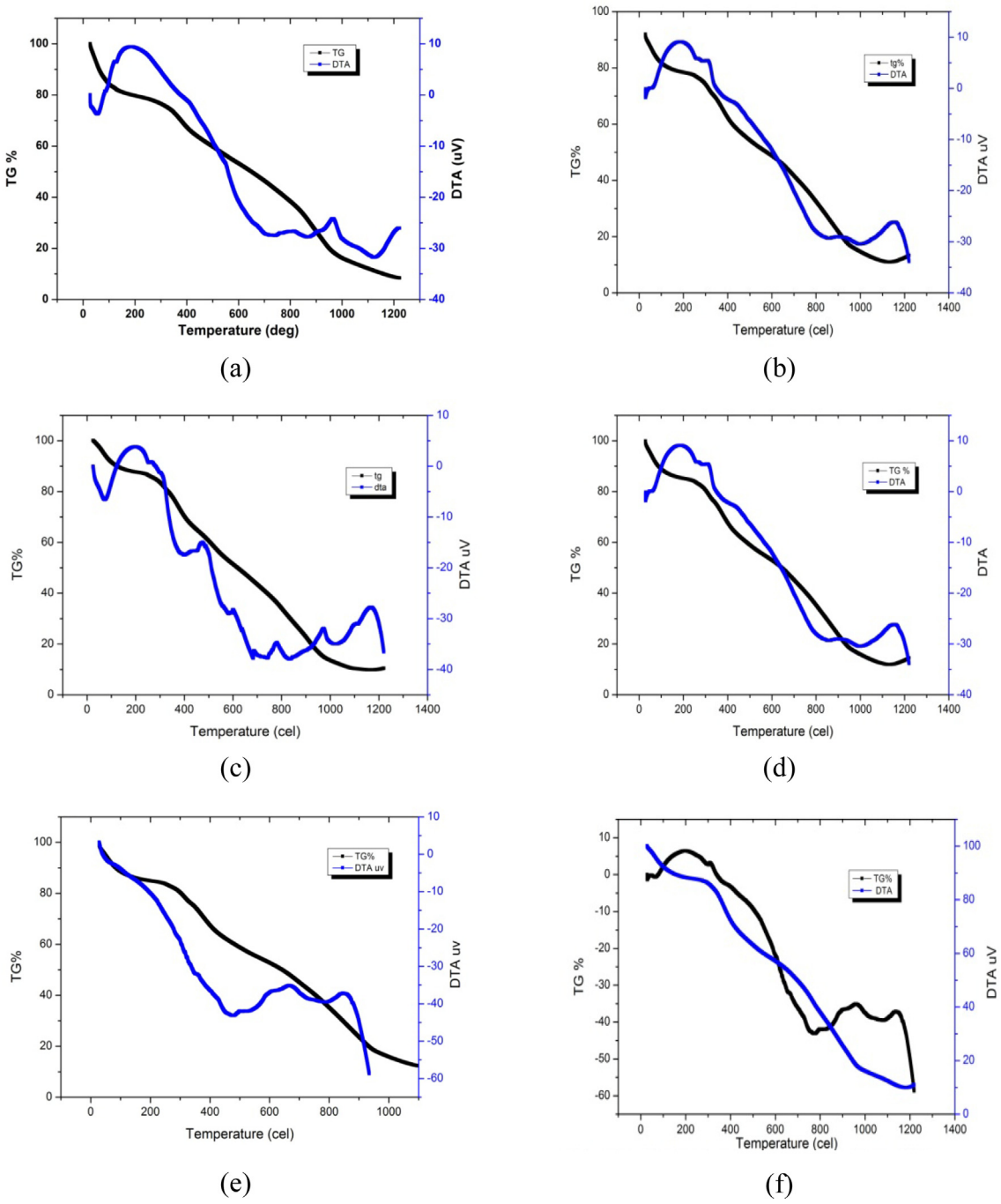

Fig. 1. TG/DTA of samples heated at 250 °C for 24 h (a) BCP (b) x = 0, (c) x = 0.04, (d) x = 0.08, (e) x = 0.16, (f) x = 0.2.

perature which may lead to evaporation of Ba, thus introduces an uncertainty of Ba content in the synthesized samples [32]. The sol gel technique can ensure the atomic level homogenous mixing of cations in the precursor stage, thus allowing the formation of the most stable structure at relatively low temperatures due to the short diffusion distance of various cations and oxygen ions.

Figs. 2a and 2b shows the XRD patterns of calcined and sintered samples. According to the Figures, a single phase perovskite with orthorhombic structure was observed which implies that Sr may be completely incorporated into the perovskite lattice structure that results in the formation of BSCZP [33–35]. All the sintered oxides displayed predominant orthorhombic perovskite structure with seven major diffraction peaks (0 0 2), (0 2 2), (2 1 3), (6 1 1), (4 2 2), (4 4 0), (6 1 3). The lattice parameters and unit cell volume are calculated from the XRD peaks using unit cell software based on the standard data of $BaCeO_3$ (JCPDS 22-0074). Partial substitution of Pr^{4+} (0.85 Å) with smaller ionic radius cations for Ce^{4+} (0.87 Å) cations of $BaCeO_3$ indicated a slight decrease in the lattice parameter and cell volume, which indicates a plane distance reduction (according to Bragg's law). The substitution of Pr is of great interest in the study due to two factors. First the ionic radius of Pr^{3+} (0.99 Å) is greater than Pr^{4+} (0.85 Å). A higher oxidation state of Pr reduces the Pr—O bond length and decreases the unit cell parameter which is consistent with the observed decrease in

Table 1
The summarisation of Thermal characteristics for dried powders (T = 250 °C).

Sample	Stage	Temperature range (°C)	Mass loss (%)	Exothermic peak (°C)	Total mass loss (%)
BCP	1	30–120	13	198	83
	2	110–630	36		
	3	630–970	34	970	
BZCP	1	30–110	10	187	75
	2	110–615	33		
	3	615–970	32	970	
BSCZP-1	1	30–120	14		84
	2	120–500	23	2,15,479	
	3	500–900	38	539	
BSCZP-2	1	30–110	11		72
	2	110–600	31	200	
	3	600–950	30	989	
BSCZP-3	1	30–100	6		81
	2	100–613	51	319	
	3	613–915	24	962	
BSCZP-4	1	30–100	8		76
	2	100–604	34	2,07,312	
	3	604–956	34	959	

the values of lattice constants [36]. Also the ionic radius of Ce^{4+} (0.87 Å) is nearer to Pr^{4+} (0.85 Å), thus makes the substitution process simple. Second from the ionic radius point of view, the bond length of Pr^{3+} is larger than Pr^{4+} in BCZP. In the case of Pr substitution the Pr^{3+}—O is found to be longer than Ce^{4+}—O but shorter than Ce^{3+}—O bond. On replacement of Ce partially by Zr^{4+} in BCY perovskite, the lattice parameters depicted a decrease owing to the fact that Zr^{4+} (0.72 Å) has a lesser ionic radius than are Ce^{4+} (0.87 Å).

On further substitution of Sr^{2+} for Ba^{2+} in the A sites, a further decrease in the lattice parameters along with cell volume with increase in the Ba deficiency is noticed which can be explained by the fact that Sr^{2+} (1.18 Å) has a smaller ionic radius than Ba^{2+} (1.2 Å) [37]. The analysis revealed a linear relation between the lattice parameters and Sr content and the average crystallite size is found to be in the range of 20–30 nm.

The crystallite sizes of the powders were calculated using Scherrer's formula. The bulk densities of the sintered pellets were resolved using Archimedes displacement method.

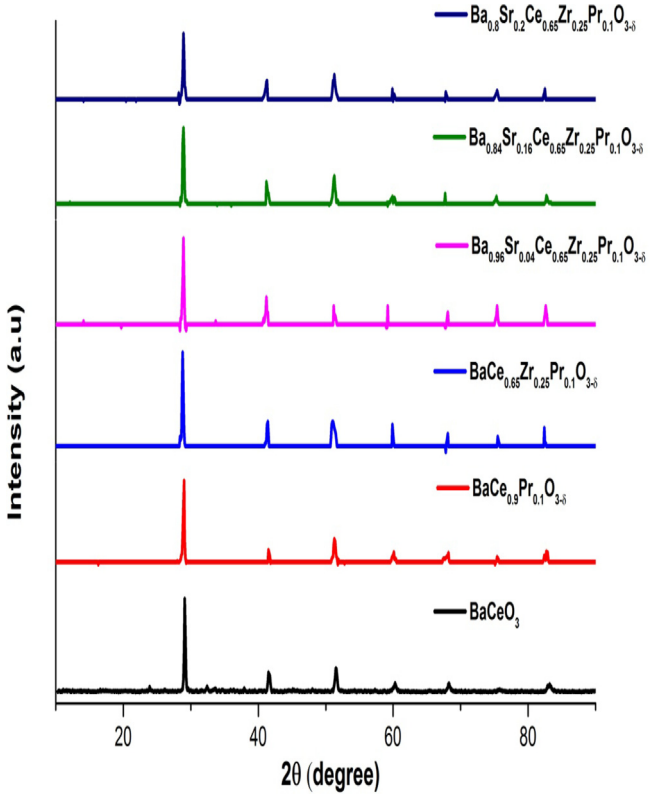

Fig. 2a. XRD pattern of calcined powders.

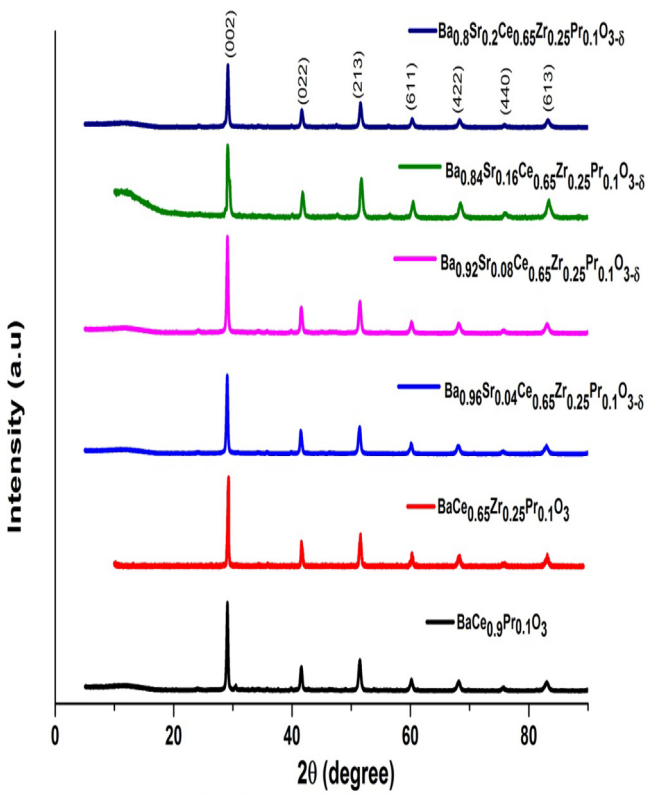

Fig. 2b. XRD pattern of sintered powders.

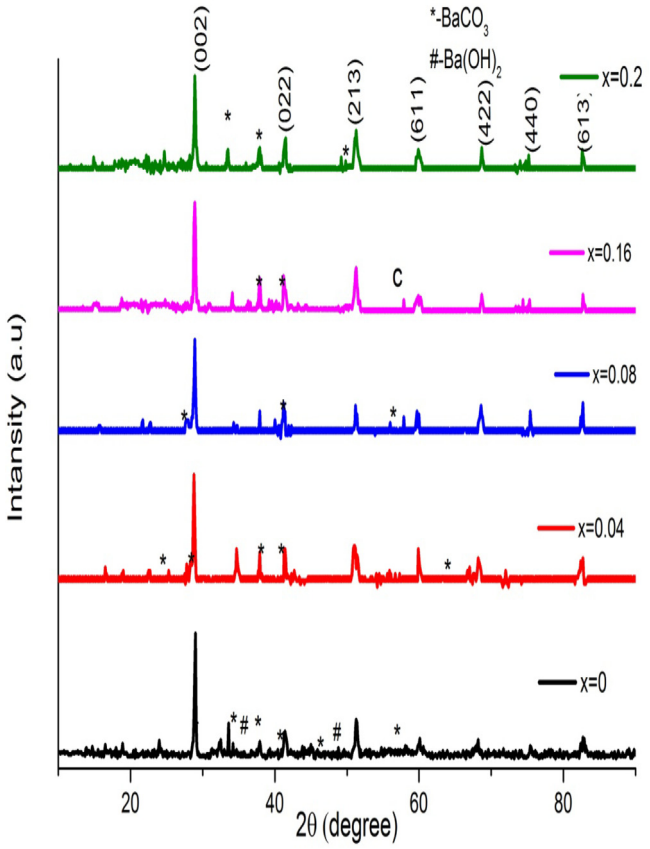

Fig. 2c. XRD pattern of sample exposed to water.

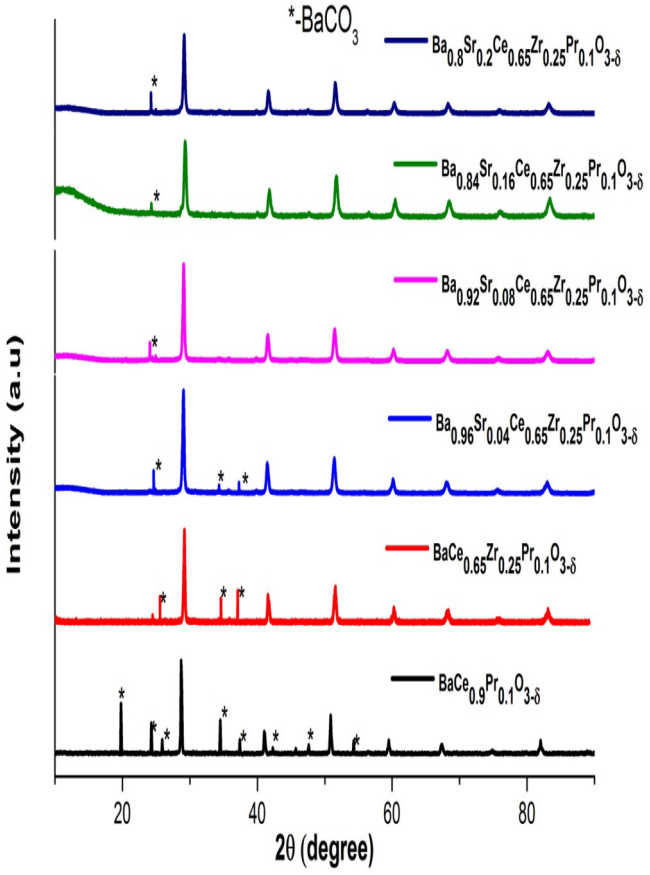

Fig. 2d. XRD pattern of sample exposed to CO_2.

Chemical stability

Barium cerate structure is not chemically stable because it can react with CO_2 according to the reaction (4) or with H_2O according to reaction (5)

$$BaCeO_3 + CO_2 \rightarrow BaCO_3 + CeO_2 \quad (4)$$

$$BaCeO_3 + H_2O \rightarrow Ba(OH)_2 + CeO_2 \quad (5)$$

In order to verify the stability under H_2O containing atmospheres, the sintered pellets are boiled in water for 2 h, dried and the XRD patterns are recorded. It has been observed that after exposed to boiling water, BCP powders decomposed to $BaCO_3$ while BCZP indicated a lesser impurity phase. A neutron diffraction study revealed that, at room temperature and pressure, in the replacement of Zr with Ce, the size of BO_6 octahedral decreases with increase in zirconium content as Zr acts as a phase stabilizer. Thus the force leading for the evolution towards a symmetric structure is increased and it becomes more difficult to distort the perovskite structure. This also show that stability in water increases with decreasing ionic radius of the co-dopant as the ionic radius of Zr^{4+} is less than Ce^{4+} [38,39]. With incorporation of Sr into the A sites partially replacing Ba, the $Ba_{1-x}Sr_xCe_{0.65}Zr_{0.25}Pr_{0.1}O_{3-\delta}$ pellets retained original perovskite structure with less additional peaks showing $BaCO_3$ phase as shown in the Fig. 2d. Due to reaction with H_2O, $BaCO_3$ may also result due to interaction with atmospheric CO_2 that converts $Ba(OH)_2$ into carbonate. The reaction product CeO_2 that may appear is insoluble in water and forms a porous layer on the surface of the $BaCeO_3$ pellet while $Ba(OH)_2$ results in a substantial volume expansion thereby forming cracks on the surface [38]. Subsequently water penetrates into the material through the cracks on the surface which resulted in the further reaction with $BaCeO_3$. The stability of the samples are found to increase with increase in the amount of Strontium into the compounds as observed from the XRD peaks shown in Fig. 2d which confirms that Ba has been successfully replaced by Sr partially.

To check the stability of the material against atmospheric CO_2 small amount is left out in the laboratory for a period of 20 days and the XRD analysis did not show any phase change except for small peaks indicating $BaCO_3$ for BCZP and BSCZP while BCP indicated $BaCO_3$ peaks as shown in Fig. 2c. These results suggested that when strontium is doped into barium cerates, it can undoubtedly improve the chemical stability of Sr doped BCZP compound. It has been reported that the stability of the perovskite structures increases with increase in the tolerance factor [25] and this is in agreement with the calculated tolerance factor and experimental lattice parameters of BSCZP when compared to the undoped tolerance factor value of $BaCeO_3$. Matsumoto et al. investigated chemical stability of $BaCeO_3$-based proton conductors doping different trivalent cations with thermo gravimetry (TG) analysis and found that stability increases with reduction in ionic size of the dopant, which correlate with the present result [40].

Scanning electron microscope and EDAX analysis

The morphological investigations of the sintered (1300 °C) powders confirmed that the sol–gel process favoured the formation of foamed structures with sub micrometer particle (1.85 to 6 μm) of sintered BCP, BCZP and BSCZP pellets. The ceramic pellets are well densified although very few pores are observed which may be due to the oxide volume shrinkage that resulted from the surface water and residual organics during high temperature treatment. The powders prepared from citrate EDTA sol gel process had a dense structure which may be due excess barium sprinkled on the platinum foil during sintering depending on the Sr content which is compensated due to barium evaporation due to high heat treatment. A small increase in the grain size is observed when Pr is

Table 2
Summary of Crystal parameters and Tolerance factor of sintered $Ba_{1-x}Sr_xCe_{0.65}Zr_{0.25}Pr_{0.1}O_{3-\delta}$ powders.

x	Crystal symmetry	a (Å)	b(Å)	c(Å)	Cell volume(Å)^3	Relative Density	Tolerance factor(t)
BCP	Orthorhombic	8.73,062	6.1530	6.21,270	333.6769	88%	0.95
0	Orthorhombic	8.73,062	6.1530	6.21,270	333.6769	88%	0.95
0.04	Orthorhombic	8.71,200	6.1470	6.1447	329.2896	85%	0.946
0.08	Orthorhombic	8.6860	6.1606	6.11,217	328.1000	87%	0.944
0.16	Orthorhombic	8.7027	6.16,066	6.11,217	327.7025	88%	0.94
0.2	Orthorhombic	8.6550	6.1410	6.1590	327.37	86%	0.938

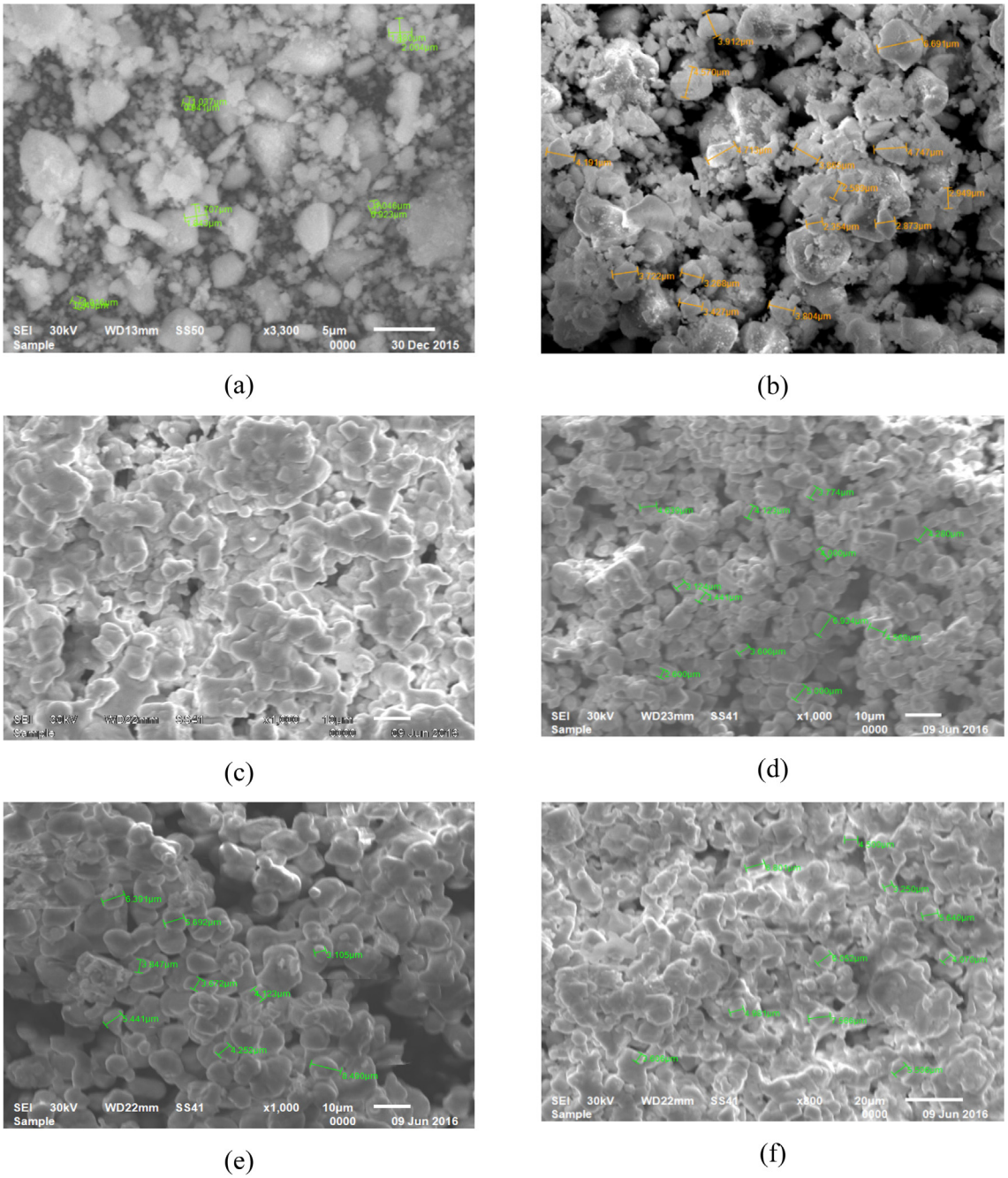

Fig. 3. SEM images of a)$BaCe_{0.9}Pr_{0.1}O_{3-\delta}$ (b)$BaCe_{0.65}Zr_{0.25}Pr_{0.1}O_{3-\delta}$ (c) $Ba_{0.96}Sr_{0.04}Ce_{0.65}Zr_{0.25}Pr_{0.1}O_{3-\delta}$ (d) $Ba_{0.92}Sr_{0.08}Ce_{0.65}Zr_{0.25}Pr_{0.1}O_{3-\delta}$ (e) $Ba_{0.84}Sr_{0.16}Ce_{0.65}Zr_{0.25}Pr_{0.1}O_{3-\delta}$ (f) $Ba_{0.8}Sr_{0.2}Ce_{0.65}Zr_{0.25}Pr_{0.1}O_{3-\delta}$.

co-doped with Ce while further Zr incorporation replacing Ce reduced the average grain size. From x = 0 to x = 0.2, a slight decrease in the grain size is observed as Sr doping increased. In order to realize the effect of Sr doping on the structural stability, the distortion of cubic lattice was calculated based on the Goldschmidt tolerance factor given in the Table 2.

Perovskite structure can be formed only with the correct selection of A site cation: B site cation: Oxygen ion ratio as predicted by Goldschmidt values of tolerance factor calculated and tabulated in Table 2. It is observed that barium atoms are too small to stabilise cubic perovskite structure with the given B site composition. Smaller Sr^{2+} when substituted into the lattice creates distortion of the crystal lattice and contributes to global lowering of symmetry of the lattice that is evident from the decrease in the tolerance factor and increase in the octahedron tilting angle. In such a deformed lattice, equilibrium sites for protons located near oxygen ions are separated by higher energy barriers than for isotropic, ideal cubic symmetry. As a result, protons become localised and macroscopic

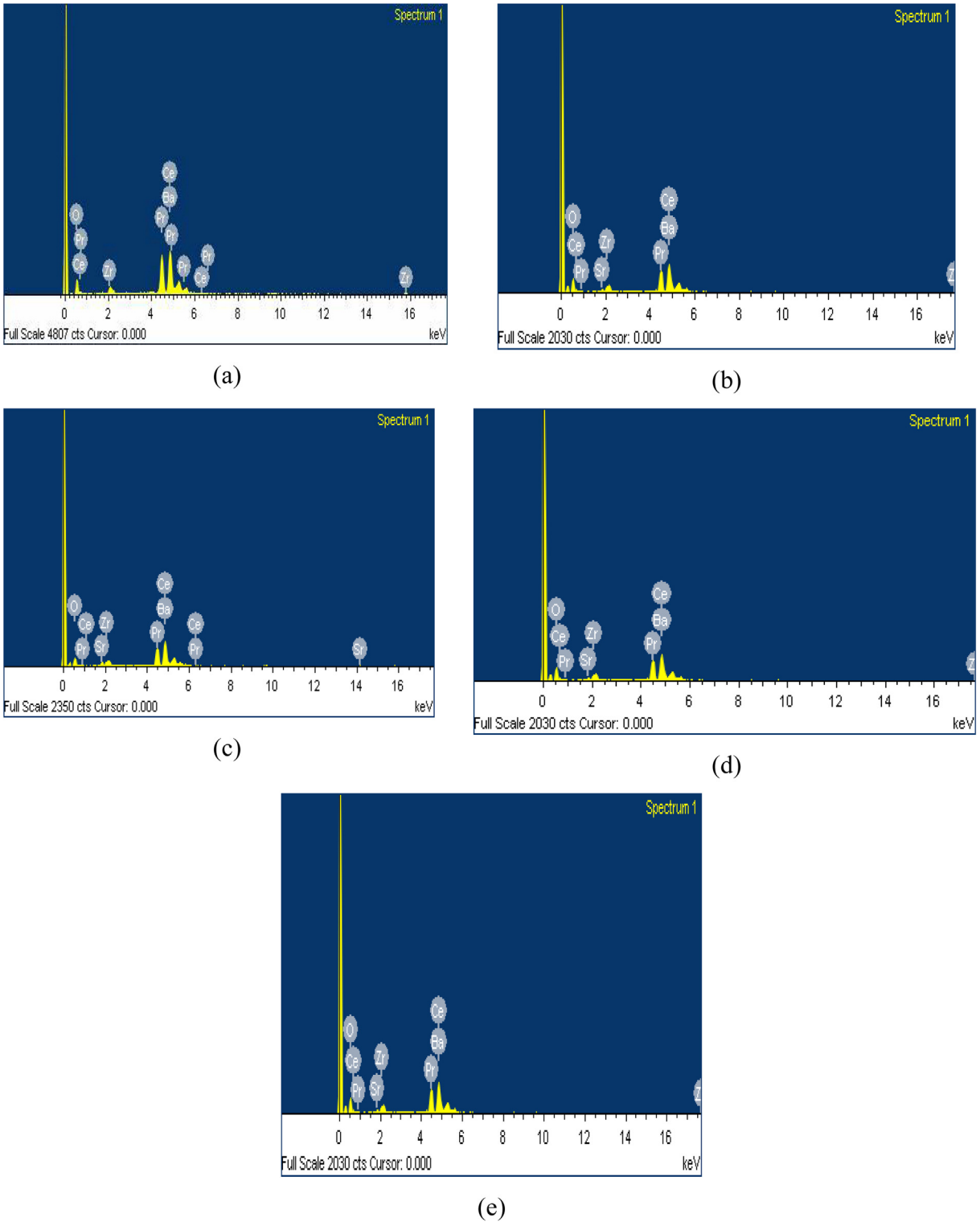

Fig. 4a. EDAX images of (a) $BaCe_{0.65}Zr_{0.25}Pr_{0.1}O_{3-\delta}$ (b) $Ba_{0.96}Sr_{0.04}Ce_{0.65}Zr_{0.25}Pr_{0.1}O_{3-\delta}$. (c) $Ba_{0.92}Sr_{0.08}Ce_{0.65}Zr_{0.25}Pr_{0.1}O_{3-\delta}$ (d) $Ba_{0.84}Sr_{0.16}Ce_{0.65}Zr_{0.25}Pr_{0.1}O_{3-\delta}$. (e) $Ba_{0.8}Sr_{0.2}Ce_{0.65}Zr_{0.25}Pr_{0.1}O_{3-\delta}$.

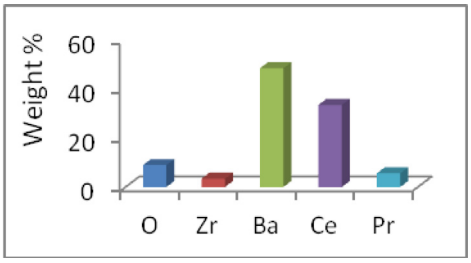

Element	Weight %	Atomic %
O	8.96	45.49
Zr	3.89	3.47
Ba	48.41	28.62
Ce	33.51	19.21
Pr	5.59	3.22

(a)

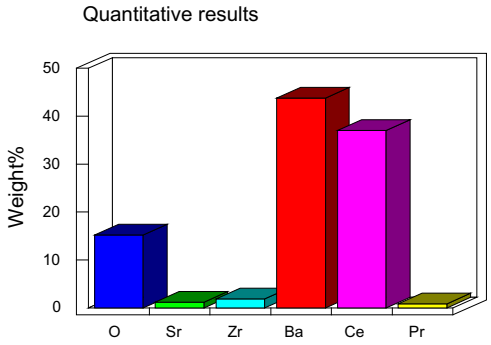

Element	Weight %	Atomic %
O	15.22	64.40
Sr	1.21	0.88
Zr	1.87	1.30
Ba	43.81	20.25
Ce	37.04	16.78
Pr	0.86	0.39

(b)

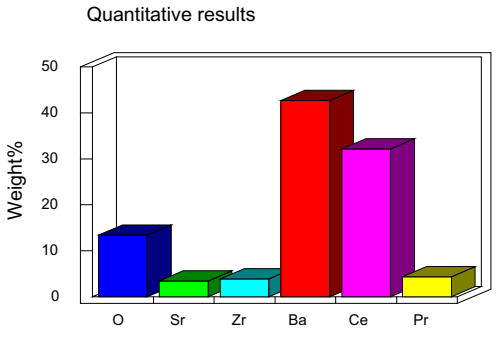

Element	Weight %	Atomic %
O	13.42	56.20
Sr	3.43	2.63
Zr	3.91	2.87
Ba	42.71	20.84
Ce	32.19	15.40
Pr	4.34	2.06

(c)

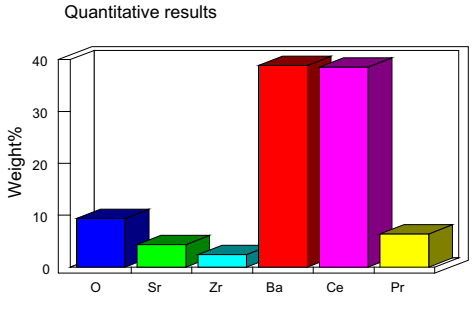

Element	Weight %	Atomic %
O	9.37	46.26
Sr	4.36	3.93
Zr	2.43	2.11
Ba	38.90	22.38
Ce	38.56	21.74
Pr	6.38	3.58

(d)

Fig. 4b. Elemental analysis of (a) $BaCe_{0.65}Zr_{0.25}Pr_{0.1}O_{3-\delta}$ (b) $Ba_{0.92}Sr_{0.08}Ce_{0.65}Zr_{0.25}Pr_{0.1}O_{3-\delta}$ (c) $Ba_{0.84}Sr_{0.16}Ce_{0.65}Zr_{0.25}Pr_{0.1}O_{3-\delta}$ (d) $Ba_{0.8}Sr_{0.2}Ce_{0.65}Zr_{0.25}Pr_{0.1}O_{3-\delta}$.

activation energy of conductivity which represents height of energy barrier increases enormously thus hindering conductivity (see Fig. 3).

EDX analysis confirmed the enrichment of Sr and Ce while depletion took place in Ba. The bulk densities of the sintered powders are calculated by the Archimedes displacement principle and theoretical density from XRD. The relative density of all the samples sintered at 1300 °C are found to be around 88% of the theoretical density and its value can be confirmed from the SEM images. Sintering at higher temperatures may further enhance the density

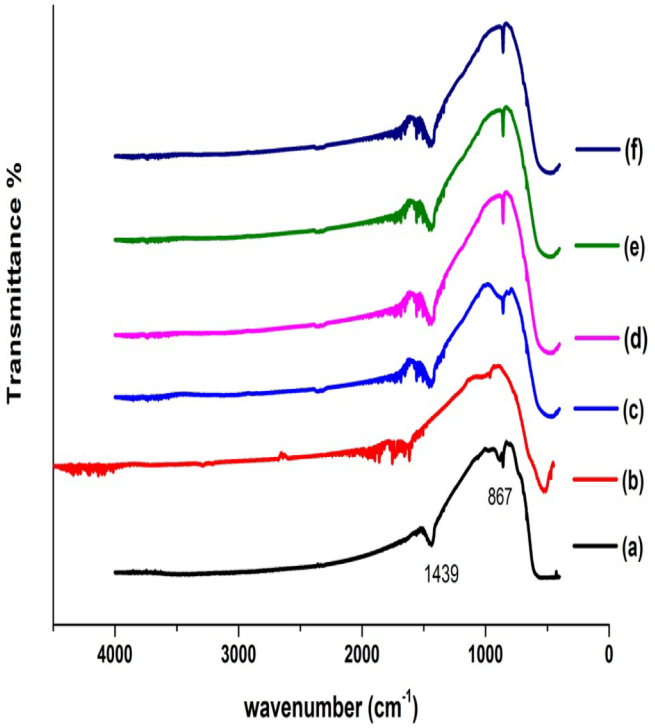

Fig. 5. FTIR spectra of (a) $BaCe_{0.9}Pr_{0.1}O_{3-\delta}$ (b) $BaCe_{0.65}Zr_{0.25}Pr_{0.1}O_{3-\delta}$ (c) $Ba_{0.96}Sr_{0.04}Ce_{0.65}Zr_{0.25}Pr_{0.1}O_{3-\delta}$ (d) $Ba_{0.92}Sr_{0.08}Ce_{0.65}Zr_{0.25}Pr_{0.1}O_{3-\delta}$ (e) $Ba_{0.84}Sr_{0.16}Ce_{0.65}Zr_{0.25}Pr_{0.1}O_{3-\delta}$ (f) $Ba_{0.8}Sr_{0.2}Ce_{0.65}Zr_{0.25}Pr_{0.1}O_{3-\delta}$.

but there may be a chance of more BaO evaporation. The aim of the present study is to find the conductivity at low sintering temperatures (see Figs. 4a and 4b).

Fourier transform infrared spectroscopy (FTIR) analysis

Fig. 5 shows the FTIR Spectra of the sintered samples. The peaks near 860–869 cm^{-1} may be assigned to the metal oxide bond between strontium and oxygen and the peaks shifted slightly to higher wave number side with increase in the Sr content (see Table 3).

All the samples exhibited a similar spectrum with a carbonate peak near 1445–1460 cm^{-1} which may be due to asymmetric C—O stretch. That may arise due to the chelation and polymerisation process resulting in the formation of metal complexes which are not observed as Sr content increased. The C—O bonding region is the indicative of organic content in the material due to the presence of residual oxides. These carbonates may not be detected by XRD because of their existence in amorphous phase in very small fractions to be detected by XRD. These values are consistent with the standard IR peaks table [41] and clearly show the complete formation of pure phase.

The increase in the absorption peak shifts to higher energy end with increase in Sr content is expected from a harmonics oscillator model that have been used to stimulate the two body stretching mode.

$$\omega_0 = \sqrt{\frac{k}{\mu}} \tag{6}$$

where ω_o is the characteristics frequency, K is Young's modulus and μ is the effective mass of the oscillator. The effective mass of (Ba—Sr)—O oscillator shrinks as Sr ions substitute Ba ions, due to the lighter atomic weight of Sr, which results in a higher characteristics frequency [42].

Raman spectroscopy studies

A Raman mapping technique is utilized to examine the local phase distribution of the $Ba_{1-x}Sr_xCe_{0.65}Zr_{0.25}Pr_{0.1}O_{3-\delta}$ oxides in this study as observed from Fig. 6. Denming and Rose proposed that a number of factors contribute to changes of Raman band position including phonon confinement, strain, particle size effect and defects. Differences in particle size led to variation in phonon relaxation and thus causes band shift. The small peak obtained in the range 100–112 cm^{-1} might be assigned to the stretching mode of the carbonate ion around the Sr ion. The Raman band around 350 cm^{-1} are $SrCeO_3$ like and 400–420 cm^{-1} are $ZrCeO_2$ like second phase and are the bending modes of ZrO_6 [43–45]. The small peak near 472 cm^{-1} may be due to Ce—O—Ce symmetric vibration due to first order scattering arise from Nd and the small peaks in the range 560–650 cm^{-1} might be attributed to the stretching mode of oxygen ion around strontium, 1490–1520 cm^{-1} may be due to $SrCO_3$ as peaks shifted to higher wave number side with increase in concentration of Sr^{2+}. The reason might be due to change in the force constants of the respective bonds and decrease of the effective atomic mass [42] which is consistent with XRD that CeO_2 like second phase diminishes with increase in Sr^{2+} content.

Impedance studies

Electrolyte conduction greatly affects the overall energy performance of high temperature solid oxide fuel cells. Here the ionic

Table 3
Comparison of the grain conductivity (σ_g) and activation energy (E_a) with the reported values.

Compound	Sintering Temperature	σ_g (S/cm)	E_a (eV)	Crystallite size(nm)	Ref.
$BaZr_{0.7}Pr_{0.1}Y_{0.2}O_{3-\delta}$	1400 °C/5 h	10^{-2}(700 °C)			[49]
$BaCe_{0.72}Y_{0.15}Pr_{0.03}O_{3-\delta}$	1600 °C/12 h	2.15×10^{-2}(500 °C)			[50]
$BaCe_{0.42}Zr_{0.4}Y_{0.15}Pr_{0.03}O_{3-\delta}$	1600 °C/12 h	1.56×10^{-2}(500 °C)			[50]
$BaCe_{0.8}Pr_{0.2}O_{3-\delta}$	1350 °C/12 h	3.07×10^{-4}(600 °C) H_2 atmosphere			[23]
$BaCe_{0.9}Pr_{0.1}O_{3-\delta}$	1300 °C/5 h	4.3×10^{-4}(500 °C) air 4.41×10^{-4}(500 °C) wet air	0.48	31	This work
$BaCe_{0.65}Zr_{0.25}Pr_{0.1}O_{3-\delta}$	1300 °C/5 h	3.5×10^{-4}(500 °C)air 3.64×10^{-4}(500 °C) wet air	0.54	30	This work
$Ba_{0.96}Sr_{0.04}Ce_{0.65}Zr_{0.25}Pr_{0.1}O_{3-\delta}$	1300 °C/5 h	3×10^{-4} (500 °C)air 3.14×10^{-4} (500 °C) wet air	0.61	29.6	This work
$Ba_{0.92}Sr_{0.08}$ $Ce_{0.65}Zr_{0.25}Pr_{0.1}O_{3-\delta}$	1300 °C/5 h	2.94×10^{-4}(500 °C)air 3.1×10^{-4}(500 °C)wet air	0.56	30	This work
$Ba_{0.84}Sr_{0.16}$ $Ce_{0.65}Zr_{0.25}Pr_{0.1}O_{3-\delta}$	1300 °C/5 h	2.83×10^{-4}(500 °C) air 2.92×10^{-4}(500 °C) wet air	0.643	29	This work
$Ba_{0.8}Sr_{0.2}Ce_{0.65}Zr_{0.25}Pr_{0.1}O_{3-\delta}$	1300 °C/5 h	2.24×10^{-4}(500 °C) air 2.47×10^{-4}(500 °C) wet air	0.65	27	This work

conductivity of the $Ba_{1-x}Sr_xCe_{0.65}Zr_{0.25}Pr_{0.1}O_{3-\delta}$ is evaluated as a function of temperature in dry air atmosphere and in wet air. The impedance spectra are measured from room temperature to 500 °C. The temperature is confined to 500 °C due to instrumental limitations and measurements at higher temperature are under process which will be reported further. The real and imaginary components of the impedance are plotted as parametric functions of frequency. Typically three arcs are observed in the plot. The arcs present at high frequencies are normally attributed to the bulk material, that present at intermediate frequencies to grain boundary behaviour and that present at low frequencies to the electrode behaviour in the Nyquist plot. The higher the temperature leads to a smaller radius of the arc, reflecting the resistance value. [46]. In the Nyquist plots of the present work as observed from Fig. 7, the high frequency and low frequency arcs could not be recognised due to the instrumental limitations of temperature and frequency. Hence the bulk response is assigned to the high frequency intercept of the medium arc with the real axis which depicted variations of about two orders of magnitude with rise in temperature from 30 to 500 °C. The semi-circular pattern represents the electrical process taking place that can be expressed in an electrical circuit with a parallel combination of resistive and capacitive elements.

The capacitance of any component depends on the relative permeability of the material and on the geometric dimensions of the three frequency regions. The obtained C values of $Ba_{1-x}Sr_x$ $Ce_{0.65}Zr_{0.25}Pr_{0.1}O_{3-\delta}$ oxide is found to be in the range of 10^{-12}F.

Ac conductivity studies

The Ac conductivity is calculated from dielectric data using the relation.

$$\sigma_{AC} = \omega\varepsilon_r\varepsilon_0 \tan\sigma \quad (7)$$

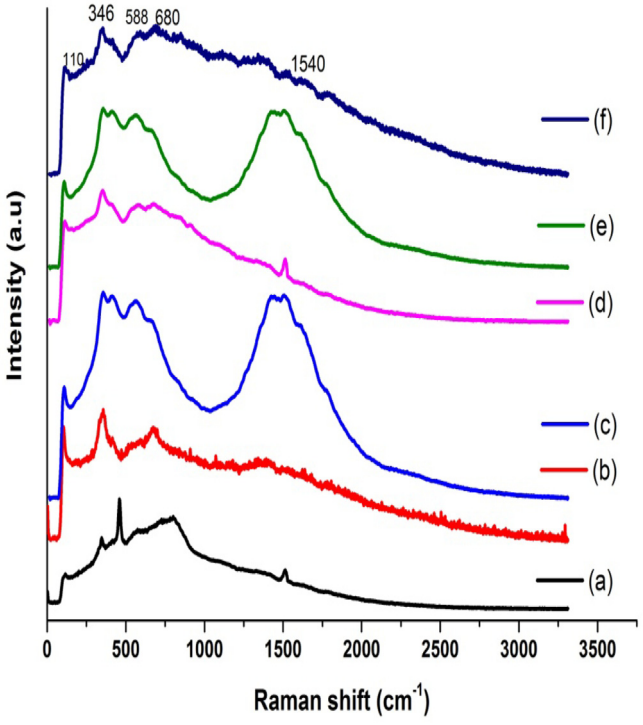

Fig. 6. Raman spectra of (a) $BaCe_{0.9}Pr_{0.1}O_{3-\delta}$ (b) $BaCe_{0.65}Zr_{0.25}Pr_{0.1}O_{3-\delta}$ (c) $Ba_{0.96}Sr_{0.04}Ce_{0.65}Zr_{0.25}Pr_{0.1}O_{3-\delta}$ (d) $Ba_{0.92}Sr_{0.08}Ce_{0.65}Zr_{0.25}Pr_{0.1}O_{3-\delta}$ (e) $Ba_{0.84}Sr_{0.16}Ce_{0.65}Zr_{0.25}Pr_{0.1}O_{3-\delta}$ (f) $Ba_{0.8}Sr_{0.2}Ce_{0.65}Zr_{0.25}Pr_{0.1}O_{3-\delta}$.

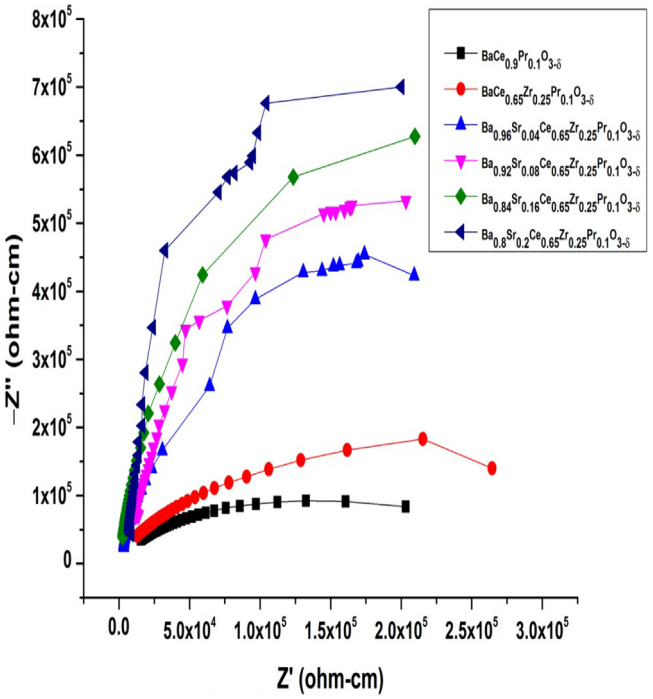

Fig. 7. Nyquist plot.

The type of temperature dependence of Ac conductivity indicates that the conduction in the material is a thermally activated process in which the motion of oxygen vacancies gives rise to an activation energy which is considered as the mobile charge carriers. The parameters such as basicity of the component metal oxides, covalency/ ionicity of the M—O bond, polarisability of the cation, and extent of dopant–hydroxyl group association etc. must also be important in determining E_σ. The level and type of conductivity of the materials depends on the nature of atoms in the A and B positions of the ABO_3 perovskite structures.

Arrhenius plots obtained from the conductivity data in air and wet atmosphere of all the samples followed a linear trend and higher values of conductivity are observed in humidified air than in dry air as show in the Fig. 8.

With respect to incorporation of a multivalent dopant such as Pr, the oxidation state changes (eg Pr^{3+} and Pr^{4+}) depending on temperature. Subsequently, two different cases can be distinguished. When Pr exists as Pr^{4}+, it does not contribute to the formation of new defects in the parent compound. When Pr exists as Pr^{3+}, it generates oxygen vacancies. In the present composition as tetravalent Pr^{4+} replaces Ce^{4+}, oxygen vacancies might be created due to the variable valance of Pr, which can become reduced from Pr^{4+} to Pr^{3+} upon exposed to H_2O. These in turn trap protons that make defect pairs to aid in the formation of electric dipoles [47]. These are responsible for the rise in the conductivity values to 4.3×10^{-4} S/cm in BCP sample at 500 °C (wet atmosphere) which is two magnitudes higher than $BaCeO_3$ (1.97×10^{-6} S/cm).

Protonic defects and oxygen vacancies are responsible for the observed mixed ionic and protonic conductivity in the present samples. As Zr is inserted into the B sites partially replacing Ce in BCP, the conductivity showed a decrease in conductivity to a value 3.5×10^{-4} and 3.64×10^{-4} S/cm at 500 °C in dry and wet atmospheres, respectively due to the slight decrease in the grain size.

On further incorporation of Sr in the A sites and with increase in the concentration of Sr, grain size decreased. As the grains became smaller in size it resulted in more grain boundary and thereby have huge contact surface of the grains representing barriers to the

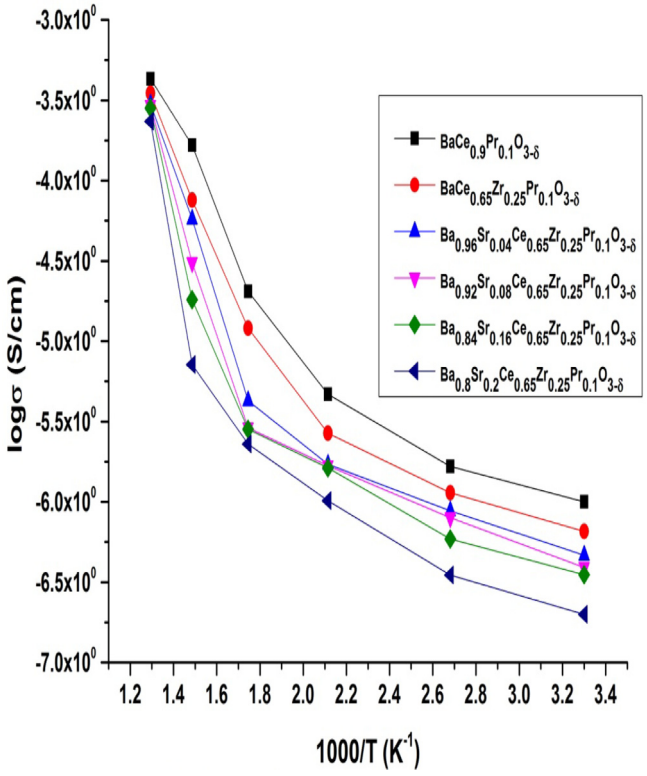

Fig. 8a. Conductivity in dry air.

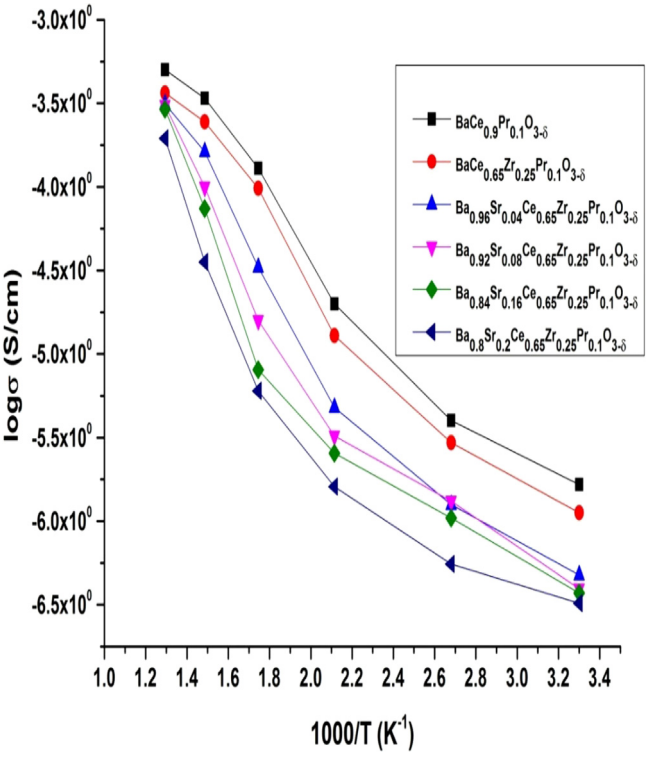

Fig. 8b. Conductivity in wet air.

transport of charged species which raises the activation energy. Also with increase in the amount of Sr, the increase in the free vacancies ceases and further dissolution might took place with the formation of associates and there might be a subsequent decrease of conductivity associated with the amount of free vacancies due to the growth of associates concentration ($R'_{Ce} - V^{\cdot\cdot}_{o}$) and ($R'_{Ce}$-$V^{\cdot\cdot}_{o} - R'_{Ce})^{x}$. Structural distortion of the perovskite system as predicted by tolerance factor, barium evaporation, non-stoichiometry and core space charge layer effect may also be possible reasons for the decrease in conductivity [48].

As expected praseodymium incorporation into the lattice increased conductivity while doping Zr and Sr into the A sites increased chemical stability. Hence this composition can be a promising electrolyte if all the values like sintering temperature, dopant concentration, relative density and time are proportionally controlled.

Dielectric constant (ε′) studies

The variation of dielectric constant with temperature (200–500 °C) and frequency (20 to 10^6 Hz) is studied. From the frequency dependent plot Fig. 9 for the sample $Ba_{0.8}Sr_{0.2}Ce_{0.65}Zr_{0.25}Pr_{0.1}O_{3-\delta}$, it was observed that the value of ε' decreases sharply with the increment in the values of frequency. All the samples reported the same trend and hence are not represented here. The higher values of dielectric constant at low frequencies can be due to space charge polarization (power frequencies) which occurs due to accumulation of charges at the interfaces in between the electrode and the sample. In low frequency regions the diploes will get adequate time to orient themselves completely along the field direction when an alternating field is applied on the sample, resulting in larger values of ε' of the samples. As the frequency increases further, the dipoles in the samples cannot reorient themselves fast enough in response to the applied electric field but lags behind, resulting in the decrease in ε' and reaches a constant value pertaining to higher frequencies applied to the sample up to 10^6 Hz.

From the plot of dielectric constant versus temperature Fig. 10, it was observed that as temperature rises, an increase is observed

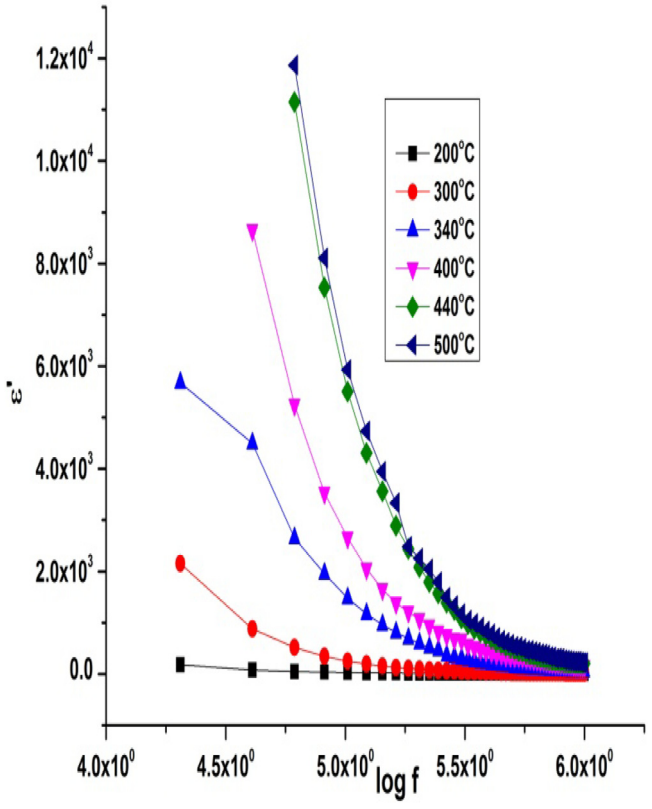

Fig. 9. Variation of real component of dielectric constant versus log f with temperature.

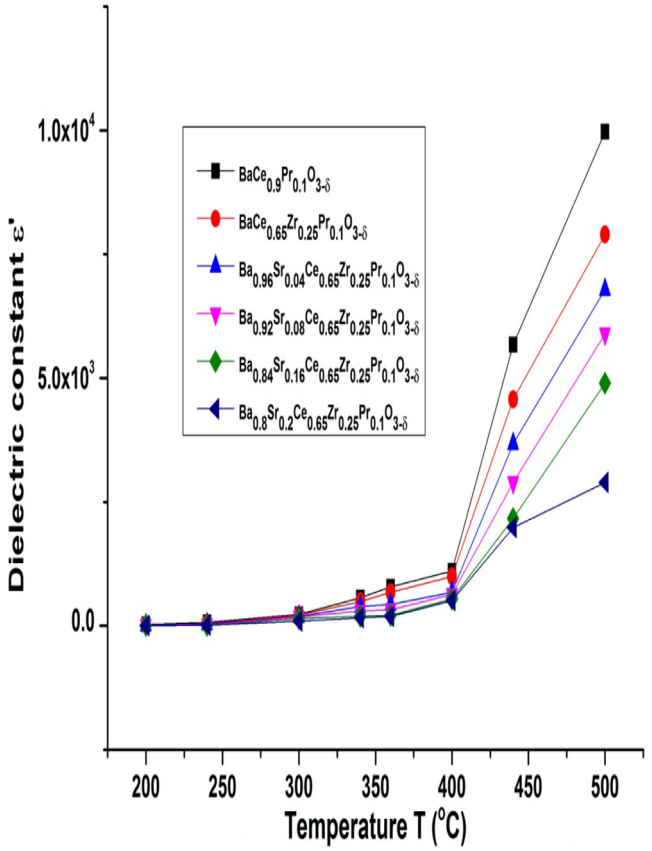

Fig. 10. Variation of dielectric constant with temperature at 1 MHz frequency.

in the dielectric constant. This can be explained as follows. In space charge polarization, diffusion of ions takes place with a rise in temperature. Additionally, thermal energy may also assist in overcoming the activation barrier for the orientation of polar molecules in the direction of the field which increases the value of ε'.

Conclusions

In this study has been systematically presented the relationship between Sr, Zr and Pr doping content and microstructure, chemical stability and conductivity of $Ba_{1-x}Sr_xCe_{0.65}Zr_{0.25}Pr_{0.1}O_{3-\delta}$ ($0 \leq x \leq 0.2$) electrolyte prepared by sol–gel method. Single phase perovskite nanostructured $Ba_{1-x}Sr_xCe_{0.65}Zr_{0.25}Pr_{0.1}O_{3-\delta}$ powders are obtained by a modified sol–gel process. The lattice constants and unit cell volumes are found to decrease as Sr atomic percentage increased in accordance with the Vegard law, confirming the formation of solid solution. Among the synthesized samples $BaCe_{0.65}Zr_{0.25}Pr_{0.1}O_{3-\delta}$ pellet with orthorhombic structure showed a conductivity with a value of 3.5×10^{-4} S/cm (dry air) & 3.64×10^{-4} S/cm (wet air with 3% relative humidity) at 500 °C. $Ba_{0.8}Sr_{0.2}Ce_{0.65}Zr_{0.25}Pr_{0.1}O_{3-\delta}$ recorded highest conductivity with a value of 2.24×10^{-4} S/cm (dry air) & 2.47×10^{-4} S/cm (wet air with 3% relative humidity) at 500 °C. All pellets with Sr exhibited good chemical stability when exposed to air and H_2O atmospheres. Comparisons with the literature showed the importance of the synthesis method on the properties of the powders. The value of relative density and conductivity obtained confirmed that higher sintering temperatures are required to increase the value of density which inturn would improve the value of conductivity. This study elucidates that $Ba_{1-x}Sr_xCe_{0.65}Zr_{0.25}Pr_{0.1}O_{3-\delta}$ composition will be a promising electrolyte for use as SOFC if Sr and Pr doping is limited to small amounts.

Acknowledgements

The authors wish to thank the Coordinator DST-Purse Programme, Advanced Analytical laboratory, Andhra University for providing XRD, SEM, FTIR and LCR measurements used in this work.

Appendix A. Supplementary data

Supplementary data associated with this article can be found, in the online version, at https://doi.org/10.1016/j.rinp.2017.11.032.

References

[1] Iwahara H, Esaka E, Uchida H, Maeda N. Solid State Ionics 1981;3:359.
[2] Iwahara H. Solid State Ionics 1996;9:86–8.
[3] Kreuer KD. Annu Rev Mater Res 2003;33:333.
[4] Guan J, Dorris SE, Liu M, Balachandran U. J Electrochem Soc 1998;145:1780.
[5] Norby T. Solid State Ionics 1990;40:849.
[6] Kreuer KD. Solid State Ionics 1999;125:285.
[7] Iwahara H, Yajima T, Habino T, Ushida H. J Electrochem Soc 1993;140:1687.
[8] Bonanos N, Ellis B, Mahmood MN. Solid State Ionics 1991;44:305.
[9] Ito N, Iijima M, Iguchi S. J Power Sources 2005;152:200.
[10] Matsumoto H, Simhura T, Higuchi T, Tanaka H, Katahira K, Otak T, et al. J Electrochem Soc 2005;152:A488.
[11] Higuchi T, Owaku T, Lida Y, Kobayashi M, Kumigashira H, Sakai E. Solid State Ionics 2015;270:1–5.
[12] Chiodelli G, Malavski C, Teald S, Barison M, Battagfrir I, Doubuo M, et al. J Alloys Compd 2009;470:447.
[13] Ryu KH, Haile SM. Solid State Ionics 1999;125:355.
[14] Katahira K, Kohichi Y, Shimura T, Iwahra H. Solid State Ionics 2000;138:91.
[15] Schober T. Solid State Ionics 2000;277:162.
[16] Fukui T, Ohara S, Kawatsu S. Solid State Ionics 1999;116:331.
[17] Li L, Wu JR, Jain R, Haile SM. Proc Electro Chem Soc 2001;12:214–23.
[18] Gorelev VP, Kuzin BL, Balakireva VB, Sharova NV, Vdovin GK, Beresnev SM, et al. Russ J Electrochem 2001;37:505.
[19] Liu Z, Cong L, Huang X, Lu Z, Su W. J. Alloys Compd. 2001;314:218.
[20] Ren Y, Li B, Wang J, Xu XJ. 2004;177:3977.
[21] Hirabayashi D, Tomita A, Brito ME, Harada T, Nagao M, Sano M. Solid State Ionics 2004;168:23.
[22] Pelletier L, McFarlan A, Maffei N. J Power Sources 2005;145:262.
[23] Basbus JF, Moreno M, Caneiro A, Mogni LV. J Electrochem Soc 2010;161(10):969–76.
[24] Escolastico S, Ivanova M, Solis C, Roitsch S, Meulenberg Wilhelm A, Jose Serra M. RSC Adv 2012;2:4932–43.
[25] Guha JP, Kolar D. J. Mater. Sci. 1971;6:1174–7.
[26] Bera J, Sarkar D. J Elec Ceram 2003;11:131–7.
[27] Weinbrunch S, Buttner H, Rosenhauer M. Phys Chem Miner 1992;19:289–97.
[28] Scholten M, Schoonman J, Van Miltenberg JC, Oonk HAJ. Solid State Ionics 1993;61:83.
[29] Deganello IF, Marchi G, Daganello G. J Eur Ceram Soc 2009;29:439–50.
[30] Wu Z, Zhou WZ, Jin W, Xu N. AICHE 2006;52:769–76.
[31] Krengvirat W, Sreekanthan S, Noor AFM, Chinwanitcharoen C, Muto H, Matsuda A. Ceram Int 2011;38:3001–9.
[32] Juo YM, Lin Y, Ran R, Shao ZP. J Power Sources 2009;193:400–7.
[33] Haile SM, Staneff G, Ryu KH. J Mater Sci 2001;36:1149–60.
[34] Barison S, Battagliarin M, Cavallin T, Daolios S, Doubova L, Fabrizio M, et al. Fuel Cells 2008:360–8.
[35] Wu J, Li LP, Espinosa WTP, Haile ST. J Mater Res 2004;19:2366–76.
[36] Hong SJ, Chang SH, Yo CH. Bull Korean Chem Soc 1979;20:54–8.
[37] Zeng Y, Mao PL, Jiang SP, Zhang L, Wu P. J Power Sources 2011;196:4524–32.
[38] Wang S, Zhao F, Zhang L, Brinkman K, Chen F. J Compd Alloys 2010;506:263–7.
[39] Wa LuJD, Wang L, Fan LH, Li H, Dai L, Guo HX. J Rare Earth 2008;26:505–10.
[40] Matsumoto H, Kawasaki Y. Electrochem Solid State Lett 2007;10:4.
[41] Osman Nafisah, Ibrahim Najwa Adni, Ishak Mohid Azlan Mohd, Hassan Oskar Hasdinor. Sains Malaysia 2014;43(9):1373–8.
[42] Denming JH, Rose SD. J Phys C Solid State Phys 1972;15:1123–33.
[43] Long RQ, Haung YP, Wan HL, Raman JJ. Spectrosc. 1997;28:29–32.
[44] Okoyama Yuji, Isa Kaori, Lee Young Sung, Sakai T. Solid State Ionics 2015;275:35–8.
[45] Kim BK, Hamaguchi HO. Phys Status Solidi (b) 1997;203:557–63.
[46] Yashiro K, Suzuki T, Kaimai A, Matsumoto H, Nigara Y, Kawada T, et al. Solid State Ionics 2004;175(1–4):341–4.
[47] Yamazaki Y, Hernandz-Sanchez R, Haile SM. J Mater Chem 2010;81:58–66.
[48] Zajac Wojciech, Hanc Emil, Gorzkowska-Sobas Agnieska, Świerczek Konrad, Molenda Janina. Solid State Ionics 2012;225:297–303.
[49] Fabbri E, Lei B, Tanaka H, Pergolesi D, Traversa E. Adv Funct Mater 2010;21:1.
[50] Melnik J, Luo J, Chuang KT, Sanger AR. Open Fuels Energy Sci J 2008;1:7–10.